ACS Photonics

Article

pubs.acs.org/journal/apchd5

Polarization-Resolved Near-Field Characterization of Nanoscale Infrared Modes in Transmission Lines Fabricated by Gallium and Helium Ion Beam Milling

Paulo Sarriugarte,[†] Martin Schnell,[†] Andrey Chuvilin,[†,‡] and Rainer Hillenbrand*[,‡,§]

[†]CIC nanoGUNE, 20018 Donostia−San Sebastian, Basque Country, Spain

[‡]IKERBASQUE, Basque Foundation for Science, 48011 Bilbao, Basque Country, Spain

[§]CIC nanoGUNE and EHU/UPV, 20018 Donostia−San Sebastian, Basque Country, Spain

ABSTRACT: We demonstrate that functional infrared transmission lines (TLs) with gap widths of 25 and 5 nm can be fabricated by gallium and helium ion beam milling of gold films thermally evaporated on insulating substrates. Interferometric and polarization-resolved scattering-type scanning near-field microscopy at $\lambda_0 = 9.3$ μm is applied to image in real space the propagation and confinement of the TL modes. Mapping the p-polarized scattered field, we obtain the distribution of the out-of-plane near-field component of the mode. When s-polarized scattered field is detected, we map the strongly confined in-plane fields propagating inside the gap. With decreasing gap width, we experimentally confirm the predicted reduction of mode diameter D_m, wavelength λ_m, and propagation length L_m. For TLs with 25 nm gap width we experimentally verify $\lambda_m = 5.1$ μm mode wavelength and $D_m = 42$ nm mode diameter ($\lambda_0/220$). The propagation length is about $L_m = 8.3$ μm, which is more than 2 orders of magnitude larger than the mode diameter; $L_m/D_m = 200$. For the TLs with a 5 nm gap we find a mode wavelength of $\lambda_m = 3.6$ μm, propagation length of $L_m = 3.9$ μm, and mode diameter of $D_m = 30$ nm. Infrared transmission lines are thus interesting candidates for the development of ultracompact infrared circuits or biochemical waveguide sensors or circuits.

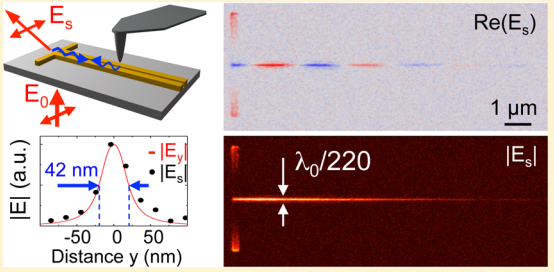

KEYWORDS: *infrared transmission lines, nanoscale infrared guiding, FIB, infrared nanophotonics, near-field microscopy*

Infrared light allows for analyzing a wide range of different material properties, particularly chemical composition.[1] Infrared spectroscopy is thus an important analytical tool in many sciences and technologies. Because of diffraction, however, the spatial resolution of conventional infrared microscopy and spectroscopy is limited to micrometers, thus preventing studies on the nanometer scale.[1,2]

An efficient route to circumvent the diffraction limit is based on plasmonic antennas[3,4] and plasmonic waveguides.[5−7] Plasmonic antennas make use of localized surface plasmon resonances (LSPRs) to efficiently convert free-space radiation into nanoscale-confined and strongly enhanced near fields, also called hot spots or nanofoci. This capability has been essential, among others, in applications such as surface-enhanced Raman spectroscopy (SERS),[8] surface- and antenna-enhanced IR absorption spectroscopy (SEIRA),[9,10] and nanoscale-resolved Fourier transform IR spectroscopy (nano-FTIR).[11] Alternatively, nanofocusing of light can be achieved by adiabatic compression of surface plasmon polaritons (SPPs) propagating on tapered metal nanowires[12−16] or slot waveguides.[17−20] The strongly confined SPP modes could find application for guiding of light on the nanoscale and in integrated plasmonics circuits[21] where SPPs are the carriers of information. At infrared or THz frequencies, where surface plasmon polaritons are generally weakly bound, specialized geometries such as corrugated metal nanowires,[22,23] coaxial waveguides,[24] or two-wire transmission lines[25,26] (TLs) improve the confinement of the SPPs, while allowing for mode propagating over several micrometers. By propagating the infrared modes along tapered two-wire TLs, the infrared energy can be compressed, yielding a nanofocus at the open end of the taper.[26,27] While these first studies promise new avenues for the development of nanoscale infrared circuits and sensor devices, extreme subwavelength-scale mid-IR guiding in sub-10 nm gaps has not been studied yet.

Here we demonstrate the fabrication of two-wire metal TLs with gap widths down to 5 nm by gallium and helium ion beam milling. By mapping the TLs with polarization and phase-resolved scattering-type scanning near-field optical microscopy (s-SNOM),[25−29] we demonstrate their function and experimentally verify extreme subwavelength-scale infrared guiding with a mode diameter of 42 nm ($\lambda_0/220$) and 8 μm propagation length for a TL with a 25 nm gap. We also discover and describe a new image contrast mechanism in s-SNOM when s-polarized light is detected: the tip acts as a local reflector of the TL mode, which is then scattered via the antenna.

TL FABRICATION BY GALLIUM AND HELIUM ION BEAM MILLING

The TLs studied in this work (Figure 1) consist of two parallel gold wires separated by an air gap of different widths g, ranging

Received: March 18, 2014
Published: June 6, 2014

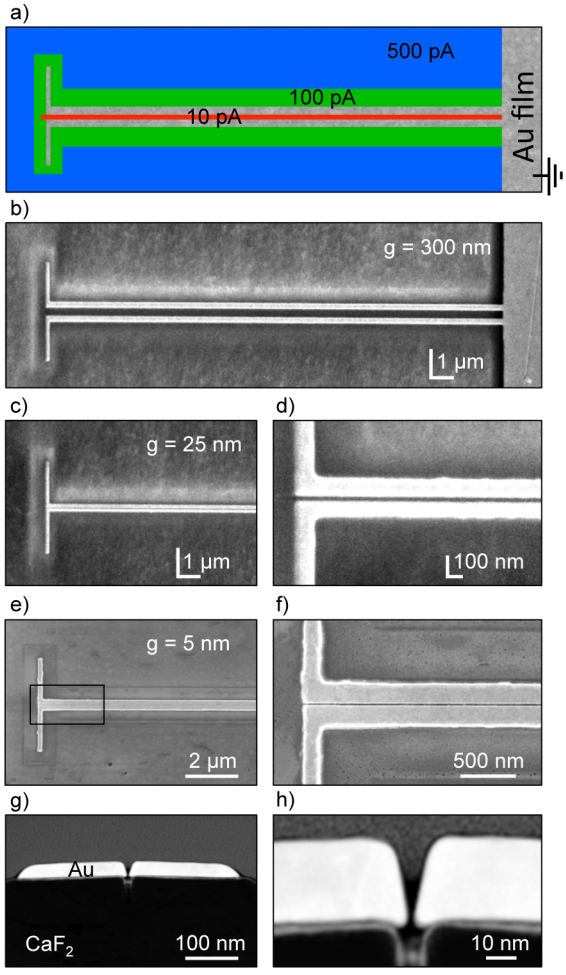

Figure 1. Sample fabrication by Ga and He ion beam milling. (a) Illustration of the three-step milling process. (b) SEM image (52° tilt) of a two-wire TL with a 300 nm wide gap with a linear antenna attached to the left end and the grounded gold layer to the right. (c) SEM image (52° tilt) of a TL with a 25 nm wide gap. (d) Zoom-in image of the TL shown in (c). (e) SEM image of a TL with a 5 nm wide gap. (f) Zoom-in image of the TL shown in (e). (g) STEM image of z cross-section of TL shown in (e), which was fabricated posterior to near-field studies. (h) Zoom-in image of the cross section shown in (g).

from 500 to 5 nm. At the end of each TL an antenna was attached for coupling far-field illumination into an antisymmetric TL mode.[25,26] CaF_2 was chosen as the supporting substrate because of its low refractive index, which increases the propagation length L_m of the TL mode compared to Si subtrates.[27] The TLs were fabricated by ion beam milling of a 40 nm thick thermally evaporated gold layer.

Employing a gallium ion beam (FEI Helios DualBeam NanoLab 600, FIB model Sidewinder) and a three-step milling process using different ion beam currents (Figure 1a), we fabricated transmission lines with gaps down to 25 nm. We first fabricated the TL contour by clearing a large area of gold with an ion beam current of 500 pA (blue area), followed by more precise milling of the contour edges at a lower current of 100 pA (green area). We then performed a single-pass line scan along the center of the TL contour at a current of 10 pA (red area) to open the gap and to produce the final TL structure (Figure 1b). Note that during the milling process the TL contour and the final TL were electrically connected to the grounded Au film, in order to avoid charging of the sample and subsequent beam deflection during the milling process, a common challenge with insulating substrates such as CaF_2. Characterizing the fabricated TLs with scanning electron microscopy (SEM) reveals a homogeneous gap along a total length of 26 μm (Figure 1b–d), which in case of the 25 nm gap (Figure 1c,d) corresponds to an aspect ratio of $>10^3$:1. Large aspect ratio gaps in combination with fast prototyping[30] are primary examples where FIB milling offers a significant advantage over e-beam fabrication processes.[31,32] To fabricate samples with narrower gaps, helium ion milling (HIM) was utilized, which has been already successfully employed for structuring silicon nitride,[33] graphene,[34,35] and magnetic spin valves.[36] Recently, its capability to fabricate sub-10 nm features in plasmonic structures has been demonstrated.[37,38]

In this work, HIM was applied to mill TL gaps below 10 nm. The helium ion milling was done with an Orion Nanofab in the Carl Zeiss Orion laboratories in Peabody (USA). First, the TL contour was fabricated with a gallium ion beam as described before. Subsequently, the gap was opened by a single-pass line scan with the helium ion beam (red area in Figure 1a). We then returned the TLs to the Helios NanoLab 600 DualBeam for nondestructive high-resolution imaging of the gap with SEM. In Figure 1e,f the gap is seen as a thin black line in the center of the TL. To measure precisely the gap width, we prepared a cross section (lamella) of the TL by focused ion beam (FIB) posterior to the near-field microscopy studies and performed scanning transmission electron microscopy (STEM). The STEM image of the cross section (Figure 1g,h) shows a wedge-shaped gap, measuring about 5 nm at the bottom of the Au film. The wedge-like shape we attribute to the ion-beam milling process. We expect more rectangular-shaped gaps for thinner gold films.

NEAR-FIELD CHARACTERIZATION BY POLARIZATION-RESOLVED INTERFEROMETRIC S-SNOM

In order to verify the IR mode propagation and field confinement in the TLs, we applied polarization-resolved transmission-mode s-SNOM[39−41] (Figure 2). The home-built s-SNOM

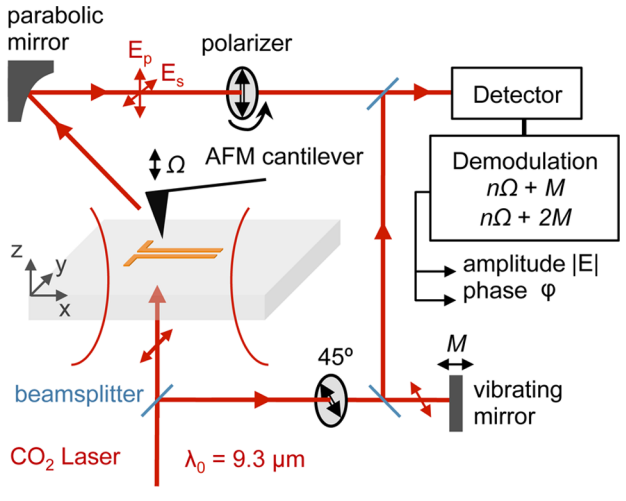

Figure 2. Transmission-mode s-SNOM setup. The sample is illuminated from below under normal incidence with a weakly focused infrared laser beam. The polarization is parallel to the antenna that is attached to the TL. The near fields at the sample surface (i.e., TL) are scattered by an AFM silicon tip and detected with a pseudoheretodyne interferometer, yielding infrared near-field amplitude and phase images by scanning the sample.

dx.doi.org/10.1021/ph500081k | ACS Photonics 2014, 1, 604−611

used in this work is based on an atomic force microscope (AFM), where commercial silicon tips (NanoWorld, Arrow-NRC-50) are employed to scatter the near fields of the TLs. The sample is illuminated from below with a weakly focused CO_2 laser beam at a wavelength of λ_0 = 9.3 μm. The polarization was chosen parallel to the dipole antenna to achieve excitation of the antisymmetric TL mode. The scattered light is collected with a parabolic mirror, analyzed with a linear polarizer to select either the p- or s-component, and detected interferometrically. Background contributions could be fully suppressed by vertical tip oscillation with a tapping amplitude of about 100 nm at a frequency of Ω = 300 kHz (tapping-mode AFM) and subsequent higher harmonic demodulation of the detector signal at 3Ω. The tip−sample distance varies in this case between 0 and 200 nm. Applying a pseudoheterodyne detection scheme[42] yields the amplitude and phase of the p- or s-component of the tip-scattered light, ($|E_p|$, φ_p) and ($|E_s|$, φ_s), respectively, depending on the polarizer orientation. We note that for imaging the sample is scanned.

For interpretation of the experimental near-field images, we compare them with numerical calculations of the near-field distribution of the TLs using a commercial FDTD software package (FDTD Solutions, www.lumerical.com). In all figures we show either the in-plane or out-of-plane component of the near-field distribution at a height of 15 nm above the TL surface. The height of 15 nm was chosen because the best agreement between experimental and calculated images was obtained (which can be well seen in Figures 5d and 6f). We attribute this finding to the finite apex radius of the Si tip (nominally around 10 nm) and the oscillating tip−sample distance.

We first mapped the TL with 25 nm gap width (SEM images in Figure 1c,d) by recording the p-polarized scattered light. Previous publications have shown that such a detection scheme yields images of the vertical (z) near-field component of antennas and transmission lines.[28,29,41,43] Figure 3a shows maps of the real part of the p-polarized scattered field, $\mathrm{Re}(E_p) = |E_p| \cos \varphi_p$. At the antenna ends we observe enhanced fields,[26] oscillating out of phase for about 180°. The fields extend along the TL wires, periodically changing their polarity and with opposite sign between the wires, providing clear evidence of a propagating, antisymmetric mode. With increasing distance x from the antenna, the propagating field decays because of dissipation in the metallic wires comprising the TLs.[25−27] From the oscillation period of the near-field patterns we can directly determine the wavelength of the TL mode, λ_m (marked by the arrow in Figure 3a). The near-field image is in excellent agreement with a numerical calculation of the real part of the vertical near-field component, $\mathrm{Re}(E_z)$ (Figure 3b), corroborating that the mapping of the p-polarized scattered light yields directly the near-field distribution of the propagating TL mode. In both experiment and calculation we find a mode wavelength of λ_m = 5.1 μm.

The near-field image contrast and underlying scattering mechanism for the p-polarized scattered field are illustrated in Figure 3c. The plane wave illumination with field E_0 excites the antenna, which subsequently launches a mode on the TL. The vertical near-field component of the TL mode induces a vertical dipole oscillation in the probing tip, resulting in scattering of a p-polarized field. Because the sample is illuminated under normal incidence and the probing tip is stationary, the phase shift of the p-polarized scattered field corresponds to the propagation phase of the TL mode. Thus, half of the TL mode wavelength is simply given by the distance between two adjacent field maxima (indicated by $\lambda_m/2$ in Figure 3a).

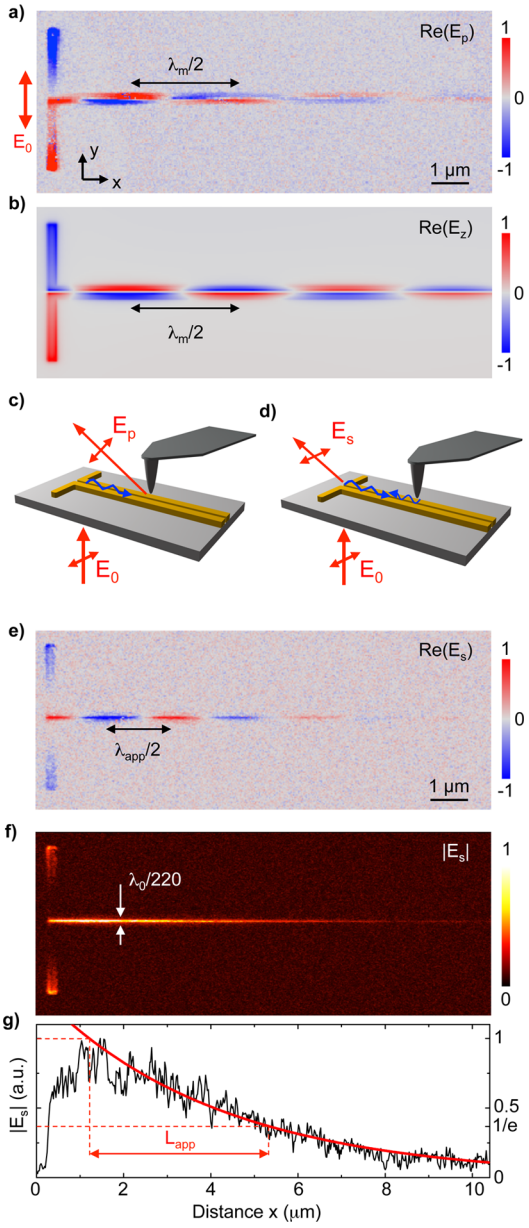

Figure 3. Near-field characterization of a TL with a 25 nm wide gap. (a) Experimental near-field image showing the real part of the p-polarized scattered field, $\mathrm{Re}(E_p)$. (b) Numerically calculated real part of the vertical near-field component, $\mathrm{Re}(E_z)$, 15 nm above the TL. (c, d) Schematics of the dominating scattering processes when p- and s-polarized scattered fields are detected, respectively. (e) Experimental near-field images showing the real part of the s-polarized scattered field, $\mathrm{Re}(E_s)$. (f) Experimental amplitude of the s-polarized scattered field $|E_s|$. (g) Near-field amplitude $|E_s|$ along the center of the TL gap, extracted from the image shown in (f). The red line shows an exponential fit, from which the apparent propagation length, L_{app}, is obtained.

We next imaged the TL with the 25 nm gap by recording the s-polarized scattered field while the TL was illuminated from below. We have previously employed this detection scheme to map the intense and strongly confined near fields ("hot spots") in antenna gaps[41] and at the apex of a tapered TL.[26] It has been shown that the near-field signal inside the gap reveals the in-plane near-field component. Here we apply this detection scheme for mapping the propagating infrared mode on two-wire TLs. In Figure 3e we show the real part of the s-polarized scattered field

dx.doi.org/10.1021/ph500081k | ACS Photonics 2014, 1, 604−611

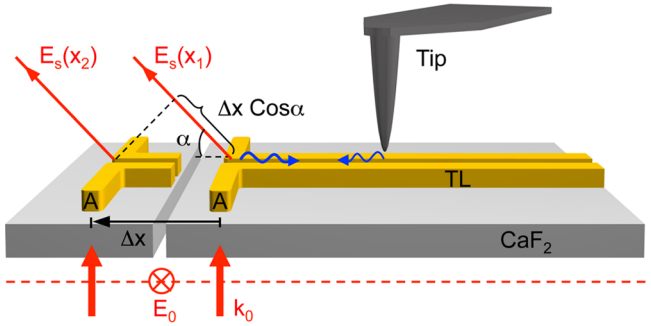

Figure 4. Model of contrast mechanism in the case where the s-polarized scattered field is recorded. Δx displays the sample displacement; α is the detection angle.

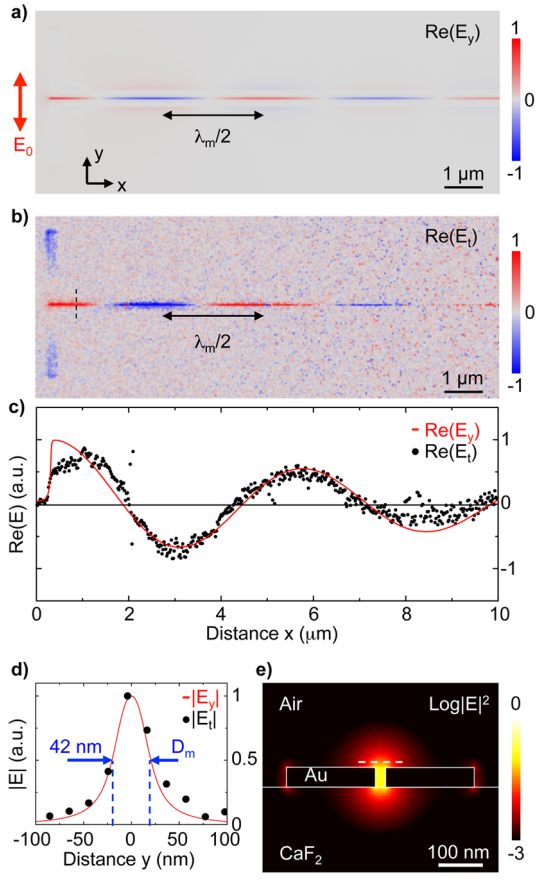

Figure 5. Reconstruction of the near-field distribution of the TL with 25 nm gap from the s-polarized scattered field. (a) Numerically calculated near-field distribution showing the real part of the in-plane field component Re(E_y), 15 nm above the TL. (b) Near-field distribution, Re(E_t), reconstructed from the experimental image in Figure 3e. (c) Real part of the reconstructed near-field distribution, Re(E_t), along the center of the TL gap, extracted from the image shown in (b). The red line shows the real part of the in-plane component, Re(E_y), calculated 15 nm above the TL gap. (d) Calculated amplitude of the in-plane near-field component, $|E_y|$ (red line), extracted along the dashed white line in (e), 15 nm above the TL. The black dots represent the experimental near-field amplitude data, $|E_t|$, extracted along the dashed black line in (b). (e) Numerically calculated mode profile, showing the normalized electric field intensity in logarithmic scale. The dashed white line indicates where the line profile shown in (d) was extracted.

(Re(E_s) = $|E_s|$ cos φ_s). We observe strong near-field signals of the same polarity at both antenna extremities, similar to former results obtained on individual infrared antennas.[44] We also see a strongly confined near-field signal along the gap between the two TL wires. The polarity of this signal oscillates along the gap, indicating that we probe the concentrated near field propagating inside the gap. Surprisingly, the apparent spatial oscillation period (marked λ_{app} in Figure 3e) is significantly shorter than λ_m in Figure 3a. This observation lets us conclude that the contrast of s-polarized near-field images is based on a different scattering mechanism. Before discussing this finding in more detail, we note that the fields decay with propagation distance, which can be better appreciated in Figure 3f, where we display the absolute value of the electric field, $|E_s|$. The field decay along the gap can be fitted by an exponential function (Figure 3g), yielding an apparent propagation length of about L_{app} = 4.15 μm.

We explain the image contrast in Figure 3e as follows. When the s-component of the scattered light is recorded, we mainly detect the s-polarized electric field scattered by the antenna attached to the TL. Because of the antenna resonance, we can assume that the s-polarized field scattered by the antenna is much stronger than the s-polarized field scattered by the dielectric tip (illustrated by the schematics in Figure 3d). We also assume that the tip causes a partial back-reflection of the TL mode, when the apex is close or inside the gap, where most of the infrared energy is expected to propagate.[26] Because of the tip vibration at frequency Ω and the nonlinear decay of the electric fields vertical to the TL, the mode reflection is modulated at harmonics of the tip vibration frequency, $n\Omega$. The reflected mode propagates back to the antenna, where it is reradiated. Recording the s-polarized scattered field by higher-order signal demodulation and pseudoheterodyne interferometric detection subsequently yields amplitude and phase maps providing information about the reflected and antenna-scattered TL mode. The amplitude signal is a measure of the strength of the mode reflection at the tip, while the phase yields the propagation phase of the TL mode. The near-field maps thus exhibit significant differences compared to near-field maps displaying the p-polarized scattered field. First, the infrared TL mode propagates twice the distance between tip and antenna before it is detected. Second, the antenna, and thus the scattering center, moves relative to the detector, which introduces a phase shift to the scattered field that depends on the sample position. For both reasons, the distance between signal maxima of the same polarity yields an apparent wavelength, λ_{app}, rather than the wavelength λ_m of the TL mode.

We note that the back-reflected TL mode does not influence the near-field images obtained for p-polarized light. First, the near-field images (particularly the mode wavelengths) match well the calculated distribution of the vertical near-field component. Second, the tip reflects the TL mode as a whole (and not a particular field component), which excites the antenna. The associated antenna radiation is s-polarized, owing to the horizontal orientation of the antenna perpendicular to the detection direction. Thus, the antenna radiation is not detected when the p-polarized scattered field is detected.

To corroborate our explanation and to reconstruct the near-field distribution of the TL from s-polarized near-field images, we developed a model describing the scattered field E_s, which is illustrated in Figure 4. We assume that the antenna launches an exponentially decaying electromagnetic mode on the TL with a mode wavelength λ_m and a propagation length L_m. The mode propagates along the TL with most of the energy confined in the gap (indicated in Figure 4 by the blue arrow on the TL pointing toward the tip). When the tip is located near the TL, the mode is partially reflected back to the antenna (indicated in

dx.doi.org/10.1021/ph500081k | ACS Photonics 2014, 1, 604−611

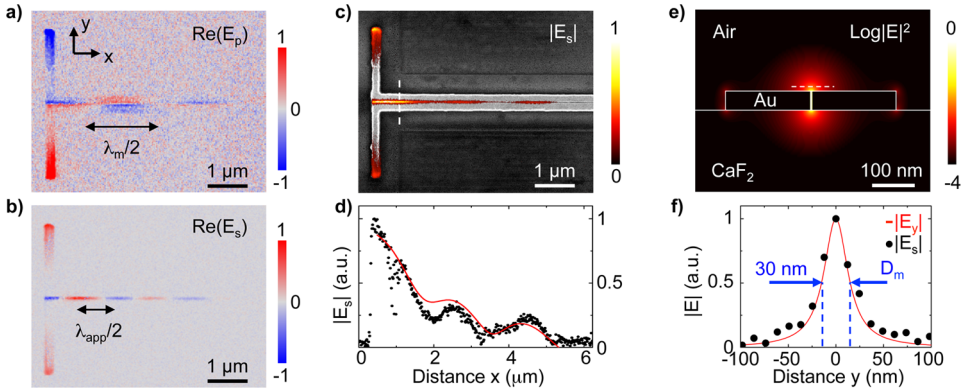

Figure 6. Near-field characterization of a TL with a 5 nm wide gap. (a) Experimental near-field image showing the real part of the p-polarized scattered field, Re(E_p). (b) Experimental near-field image showing the real part of the s-polarized scattered field, Re(E_s). (c) Experimental near-field amplitude image (color) of the s-polarized scattered field $|E_s|$, superposed to the SEM image (in gray) of the TL. (d) Experimental near-field amplitude (black dots) along the center of the TL gap, extracted from the near-field image shown in (c). The red line represents a fit to the data, assuming an exponentially decaying wave being back-reflected at position $x = 5$ μm. (e) Numerically calculated mode profile, showing the normalized electric field intensity in logarithmic scale. (f) Calculated amplitude of the in-plane near-field component, $|E_y|$ (red line), extracted along the dashed white line in (e), 15 nm above the TL. The black dots represent the experimental near-field amplitude data, $|E_s|$, extracted from (c) along the dashed white line.

Figure 4 by the blue arrow on the TL pointing toward the antenna), where it is radiated. Assuming that the mode has an initial field E_0 (i.e., $E_t(x = 0) = E_0$), the field at the tip (located on the TL gap at distance x from the antenna) is then given by

$$E_t(x, y) \propto E_0 e^{i2\pi x/\lambda_m} e^{-x/L_m} \quad (1)$$

and the back-reflected field at the antenna by $E_t(2x, y)$. To finally obtain the scattered field, we have to account for the sample (antenna) movement relative to the detector, given by the last exponent in eq 2:

$$E_s(x, y) = E_t(x, y)\, e^{i2\pi x/\lambda_m}\, e^{-x/L_m} e^{-i2\pi x \cos\alpha/\lambda_0} \quad (2)$$

λ_0 is the wavelength of the free-space radiation and $\alpha = 30°$ the angle of detection relative to the sample surface. In the near-field map, the scattered field subsequently yields an apparent near-field distribution given by

$$E_{app}(x, y) \propto E_0\, e^{i2\pi x/\lambda_{app}}\, e^{-x/L_{app}} \quad (3)$$

Comparing eqs 2 and 3, we obtain the mode wavelength and propagation length:

$$\lambda_m = \frac{2\lambda_0\lambda_{app}}{\lambda_0 + \lambda_{app}\cos\alpha} \quad (4)$$

and

$$L_m = 2L_{app} \quad (5)$$

With an apparent wavelength of $\lambda_{app} = 3.1$ μm (Figure 3e), we obtain $\lambda_m = 4.9$ μm, which is in good agreement with the mode wavelength obtained directly from Figure 3a ($\lambda_m = 5.1$ μm) and with numerically calculated results (see Figure 7a and discussion below). For the propagation length we obtain $L_m = 8.3$ μm, which is slightly shorter than the numerically calculated propagation length (see Figure 7b and discussion below).

Having measured both amplitude and phase of the scattered field $E_s(x, y)$, we can reconstruct the near-field distribution of the TL. Using eq 2, $\lambda_{app} = 3.1$ μm from Figure 3e, and $L_{app} = 4.15$ μm from Figure 3f, we obtain $E_t(x, y)$. The real part of $E_t(x, y)$ is shown in Figure 5b. It matches well with the numerically calculated near-field distribution (real part of $E_y(x, y)$) of the TL shown in Figure 5a. The good agreement can be further appreciated in Figure 5c, which shows the reconstructed (dots) and numerically calculated (red line) field along the TL gap.

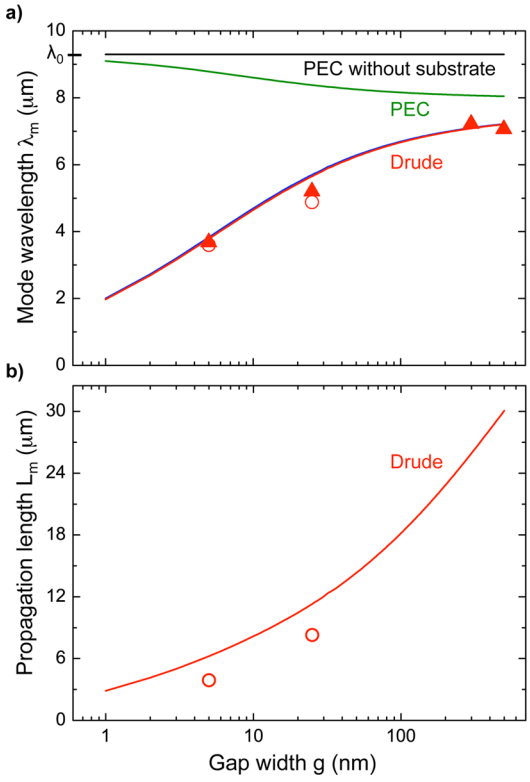

Figure 7. Propagation properties of TL modes. (a) Calculated wavelength of the TL mode as a function of the gap width g. Red line: TL made of Au described by the Drude model. Green line: TL made of PEC. Black line: TL made of PEC and without substrate. The red triangles display the experimental data extracted from Figures 3a and 6a and from images (not shown) of vertical near-field distribution of TLs with 300 and 500 nm gap width. The red circles display the mode wavelength reconstructed from the data shown in Figures 3e and 6b. (b) Calculated propagation length of the TL mode as a function of the gap width g, for a TL made of Au described by the Drude model. The red circles display the experimental propagation lengths obtained from the fittings shown in Figures 3g and 6d.

dx.doi.org/10.1021/ph500081k | ACS Photonics 2014, 1, 604−611

In Figure 5d we display the near-field amplitude along the dashed black line in Figure 5b in order to measure the mode diameter D_m. As mode diameter we define the full width at half maximum (FWHM) of the measured near-field profile perpendicular to the TL gap. We find a mode diameter D_m of about 42 nm, which is significantly smaller than the incident wavelength λ_0 (λ_0/D_m = 220), providing direct experimental evidence of nanoscale field confinement that can be achieved with TLs at IR frequencies. For comparison, we show the calculated near-field profile in 15 nm height above the TL, which has been extracted from Figure 5e. As can be seen in Figure 5d, the calculated field profile (black solid line) matches well with the measured near-field profile (symbols).

Comparing propagation length and mode wavelength, we find $L_m/\lambda_m \approx 1.7$, which seems rather short. However, by comparing the propagation length with the mode diameter D_m = 42 nm (Figure 5d), we obtain the quite large value L_m/D_m = 8.3 μm/42 nm = 200. Remarkably, a mid-IR mode with a diameter less than 50 nm can propagate several micrometers. The large difference between the two relative propagation lengths, L_m/λ_m and L_m/D_m, is due to the rather long wavelength of the mode, being 2 orders of magnitude larger than the mode confinement. We stress that nanoscale field confinement does not require ultrashort mode wavelengths, as we discuss in more detail below.

We also imaged the TL with a 5 nm gap width by recording the p- and s-polarized scattered field. The images showing the real part of E_p and E_s are displayed in Figure 6a and b, respectively. As before in Figure 3 with the 25 nm gap TL, we observe an oscillating near-field distribution on the TL. For the s-polarization, the detected (apparent) wavelength is significantly shorter than with the p-polarization due to the different scattering mechanisms, as explained above. The images clearly demonstrate that the He-milled TL with only a 5 nm gap width is functional and supports a highly confined infrared mode. In Figure 6a we directly measure λ_m = 3.68 μm, while in Figure 6b we find λ_{app} = 2.2 μm, yielding λ_m = 3.6 μm according to eq 4. λ_m is thus about 30% shorter than the one measured in Figure 3a for the TL with 25 nm gap width. We discuss this gap-dependent wavelength reduction below in Figure 7a.

We note that the near field in both Figure 6a and b abruptly vanishes at about 5 μm distance from the antenna. This can be explained by a short circuit in the transmission line (eventually by incomplete milling of the gap or formation of a metal bridge due to resputtering of the gold), which becomes evident by displaying the amplitude of the s-polarized scattered field in Figure 6c. We observe modulations of the field amplitude along the gap, rather than a monotonic exponentially decaying field. We explain them as interference between the forward propagating mode and the mode that is back-reflected at the short circuit. In order to obtain the propagation length L_m, we averaged the line scans around the gap in Figure 6c and fitted the result to a damped standing wave (red solid line in Figure 6d). We obtain a propagation length of L_m = 3.9 μm, which is slightly smaller than the numerically calculated propagation length $L_{m,calc}$ = 6.2 μm (see Figure 7b).

In Figure 6f we display the near-field profile along the dashed white line in Figure 6c. We find a FWHM of about 30 nm, which indicates a mode diameter being about 310 times smaller than the incident wavelength λ_0, respectively 120 times smaller than the mode wavelength; λ_m/D_m = 120. For comparison, we show the calculated near-field profile at 15 nm height above the TL, which has been extracted from Figure 6e. As can be seen in Figure 6f, the calculated field profile (red line) matches well with the measured near-field profile (black dots). Comparing the propagation length with the mode diameter D_m = 30 nm (Figure 6f), we obtain L_m/D_m = 3.9 μm/30 nm = 130, which is slightly smaller than the one obtained for the TL with gap width g = 25 nm.

STUDY OF MODE PROPERTIES AS A FUNCTION OF GAP WIDTH

In Figure 7a we summarize the experimentally found mode wavelengths λ_m (symbols) as a function of the gap width g and compare them with results obtained by numerical calculations (red solid line) performed with a mode solver (FDTD Solutions, www.lumerical.com). The experimental values for g = 300 and 500 nm were taken from near-field images not shown, and the ones for g = 5 and 25 nm were taken from Figures 3a and 6a (red triangles) and reconstructed from Figures 3e and 6b (red circles). In the calculations we considered infinitely long TLs consisting of two rectangular Au wires (width 200 nm, height 40 nm) separated by a rectangular-shaped gap of width g and supported by a CaF_2 substrate. To describe gold at mid-IR frequencies, we used the Drude model, yielding the permittivity

$$\varepsilon_{Au}(\omega) = \varepsilon_{inf} - \frac{\omega_p^2}{\omega^2 + i\Gamma\omega} \quad (6)$$

with ω_p = 8.95 eV being the plasma frequency, Γ = 65.8 meV the damping parameter, and ε_{inf} = 11.[45] Employing the dielectric values for λ_0 = 9.3 μm, we obtain good quantitative agreement between calculated (red solid line) and experimental (symbols) mode wavelengths λ_m. Particularly, the plot corroborates that λ_m decreases with decreasing gap width g, reaching values of about $\lambda_0/5$ for gaps as small as 1 nm.

In order to understand the wavelength reduction of two-wire TL modes at mid-infrared frequencies (that is, far away from the strong plasmonic behavior of gold), we performed mode simulations where we assumed artificial material properties for the gold. First, we assume that gold is a lossless Drude metal; that is, we set the damping parameter in the Drude model (eq 6) to zero (Γ = 0). The calculated mode wavelengths in this case (blue curve in Figure 7a) are nearly identical to the mode wavelengths obtained by using a realistic Drude model for gold (red curve in Figure 7a). This finding indicates that the absorption in the gold is not the cause for the mode wavelength reduction. By substituting Au by a perfect electric conductor (PEC) in the calculations, the mode wavelength λ_m does not decrease but slightly increases with decreasing gap width, approaching λ_0 for g < 100 nm (green curve in Figure 7a). This is because for a PEC material no field is propagating inside the wires. The fields propagate in the air and the substrate below the TL. When the gap width is reduced, the field concentrates inside the air gap, and thus a smaller part of the mode propagates in the substrate. For that reason, the mode wavelength λ_m increases for smaller gaps, approaching the mode wavelength λ_0 of a PEC without substrate (black curve in Figure 7a). Note that for a PEC TL without substrate all field energy propagates in air, and thus the mode wavelength λ_m equals λ_0 for all gap widths. From the sum of all these numerical results we conclude that in a realistic gold TL the mode wavelength λ_m decreases because of an increasing amount of field energy propagating inside the gold when the gap width decreases, owing to the finite real part of the dielectric function. This effect has been already described analytically for nanoscale plasmon cavities.[46]

It is worth noting that the mode wavelength λ_m for sub-10 nm gaps is still in the micrometer range, showing that nanoscale field

dx.doi.org/10.1021/ph500081k | ACS Photonics 2014, 1, 604−611

confinement in infrared TLs (as observed in Figures 5e and 6d) does not require wavelength compression to the nanometer scale. The mechanism of field confinement in the TLs is rather of geometrical nature. The two metal wires (Au or PEC) are the mode carriers, and the field confinement is achieved by capacitive coupling between the TL wires.[13]

We also calculated the mode propagation length L_m as a function of gap width g. The results are shown in Figure 7b together with the experimental values for g = 25 nm and g = 5 nm obtained from the fittings shown in Figures 3g and 6d. The experimental values are in good agreement with the calculated ones, although the experimental propagation lengths are slightly smaller. These discrepancies might be explained by imperfections in the fabrication process, such as ion implantation and ion beam damage of gold and substrate, or due to nonuniformity of the gap width. We note that the numerical calculations predict significant propagation distances even for TLs with sub-5 nm gaps; for example L_m = 3 μm for g = 1 nm.

SUMMARY AND CONCLUSIONS

We demonstrated that focused ion beam milling can be applied for fabricating functional mid-infrared two-wire transmission lines on insulating substrates. By applying Ga and He ion beam milling we could fabricate metal TL wires separated by air gaps as small as 5 nm. Employing polarization-resolved interferometric s-SNOM, we could experimentally map the near-field distribution, wavelength, and confinement of the mid-infrared modes supported by the TLs. Numerical simulations confirm the experimental results, corroborating that nanoscale mid-infrared mode confinement and micrometer long propagation distances can be achieved with such TLs. The ratio between propagation distance and mode confinement is larger than 100, which makes metal two-wire transmission lines promising structures for guiding and manipulating mid-infrared energy in nanoscale circuits and devices. TLs comprising nanoscale wire separation thus could become highly valuable building blocks in ultrasensitive and ultracompact mid-infrared sensing, spectroscopy, and nanoimaging applications.

AUTHOR INFORMATION

Corresponding Author

*E-mail: r.hillenbrand@nanogune.eu.

Notes

The authors declare the following competing financial interest(s): R.H. is co-founder of Neaspec GmbH, a company producing scattering-type scanning near-field optical microscope systems. All other authors declare no competing financial interests.

ACKNOWLEDGMENTS

We acknowledge financial support from FEI Company (The Netherlands) within the framework of a collaborative project. We also acknowledge Carl Zeiss NTS, LLC (Peabody, USA) for helium ion beam milling with the Carl Zeiss Orion Nanofab. This work was further supported by the National Project MAT2012-36580 from the Spanish Ministerio de Economía y Competitividad and the Etortek IE11-304 program by the Department of Development and Competitiveness of the Basque Government and by the ERC Starting Grant No. 258461 (TERATOMO). P.S. acknowledges financial support from "Ikertzaileen Prestakuntza eta Hobekuntzarako Programa" and A.C. from the project CTP11-P14, both from the Department of Education, Universities and Research of the Basque Government.

REFERENCES

(1) Griffiths, P. R.; de Haseth, J. A. *Fourier Transform Infrared Spectrometry*; John Wiley & Sons: Hoboken, NJ, 2007.
(2) Born, M.; Wolf, E. *Principles of Optics*; Cambridge University Press: Cambridge, 1999.
(3) Mühlschlegel, P.; Eisler, H.-J.; Martin, O. J. F.; Hecht, B.; Pohl, D. W. Resonant Optical Antennas. *Science* **2005**, *308*, 1607−1609.
(4) Novotny, L. Effective Wavelength Scaling for Optical Antennas. *Phys. Rev. Lett.* **2007**, *98*, 266802.
(5) Weeber, J.-C.; Krenn, J.; Dereux, A.; Lamprecht, B.; Lacroute, Y.; Goudonnet, J. Near-Field Observation of Surface Plasmon Polariton Propagation on Thin Metal Stripes. *Phys. Rev. B* **2001**, *64*, 045411.
(6) Maier, S. A.; Kik, P. G.; Atwater, H. A.; Meltzer, S.; Harel, E.; Koel, B. E.; Requicha, A. A. G. Local Detection of Electromagnetic Energy Transport below the Diffraction Limit in Metal Nanoparticle Plasmon Waveguides. *Nat. Mater.* **2003**, *2*, 229−232.
(7) Bozhevolnyi, S. I.; Volkov, V. S.; Devaux, E.; Laluet, J.-Y.; Ebbesen, T. W. Channel Plasmon Subwavelength Waveguide Components Including Interferometers and Ring Resonators. *Nature* **2006**, *440*, 508−511.
(8) Moskovits, M. Surface-Enhanced Spectroscopy. *Rev. Mod. Phys.* **1985**, *57*, 783−826.
(9) Neubrech, F.; Pucci, A.; Cornelius, T.; Karim, S.; García-Etxarri, A.; Aizpurua, J. Resonant Plasmonic and Vibrational Coupling in a Tailored Nanoantenna for Infrared Detection. *Phys. Rev. Lett.* **2008**, *101*, 157403.
(10) Adato, R.; Yanik, A. A.; Amsden, J. J.; Kaplan, D. L.; Omenetto, F. G.; Hong, M. K.; Erramilli, S.; Altug, H. Ultra-Sensitive Vibrational Spectroscopy of Protein Monolayers with Plasmonic Nanoantenna Arrays. *Proc. Natl. Acad. Sci. U.S.A.* **2009**, *106*, 19227−19232.
(11) Huth, F.; Govyadinov, A.; Amarie, S.; Nuansing, W.; Keilmann, F.; Hillenbrand, R. Nano-FTIR Absorption Spectroscopy of Molecular Fingerprints at 20 nm Spatial Resolution. *Nano Lett.* **2012**, *12*, 3973−3978.
(12) Babadjanyan, A. J.; Margaryan, N. L.; Nerkararyan, K. V. Superfocusing of Surface Polaritons in the Conical Structure. *J. Appl. Phys.* **2000**, *87*, 3785−3788.
(13) Stockman, M. Nanofocusing of Optical Energy in Tapered Plasmonic Waveguides. *Phys. Rev. Lett.* **2004**, *93*, 137404.
(14) Ropers, C.; Neacsu, C. C.; Elsaesser, T.; Albrecht, M.; Raschke, M. B.; Lienau, C. Grating-Coupling of Surface Plasmons onto Metallic Tips: A Nanoconfined Light Source. *Nano Lett.* **2007**, *7*, 2784−2788.
(15) Verhagen, E.; Spasenović, M.; Polman, A.; Kuipers, L. Nanowire Plasmon Excitation by Adiabatic Mode Transformation. *Phys. Rev. Lett.* **2009**, *102*, 203904.
(16) De Angelis, F.; Das, G.; Candeloro, P.; Patrini, M.; Galli, M.; Bek, A.; Lazzarino, M.; Maksymov, I.; Liberale, C.; Andreani, L. C.; Di Fabrizio, E. Nanoscale Chemical Mapping Using Three-Dimensional Adiabatic Compression of Surface Plasmon Polaritons. *Nat. Nanotechnol.* **2010**, *5*, 67−72.
(17) Dionne, J.; Sweatlock, L.; Atwater, H.; Polman, A. Plasmon Slot Waveguides: Towards Chip-Scale Propagation with Subwavelength-Scale Localization. *Phys. Rev. B* **2006**, *73*, 035407.
(18) Pile, D. F. P.; Gramotnev, D. K. Adiabatic and Nonadiabatic Nanofocusing of Plasmons by Tapered Gap Plasmon Waveguides. *Appl. Phys. Lett.* **2006**, *89*, 041111.
(19) Choi, H.; Pile, D. F.; Nam, S.; Bartal, G.; Zhang, X. Compressing Surface Plasmons for Nano-Scale Optical Focusing. *Opt. Express* **2009**, *17*, 7519−7524.
(20) Vedantam, S.; Lee, H.; Tang, J.; Conway, J.; Staffaroni, M.; Yablonovitch, E. A Plasmonic Dimple Lens for Nanoscale Focusing of Light. *Nano Lett.* **2009**, *9*, 3447−3452.
(21) Engheta, N. Circuits with Light at Nanoscales: Optical Nanocircuits Inspired by Metamaterials. *Science* **2007**, *317*, 1698−1702.
(22) Maier, S.; Andrews, S.; Martín-Moreno, L.; García-Vidal, F. Terahertz Surface Plasmon-Polariton Propagation and Focusing on Periodically Corrugated Metal Wires. *Phys. Rev. Lett.* **2006**, *97*, 176805.
(23) Bousseksou, A.; Babuty, A.; Tetienne, J.; Braive, R.; Beaudoin, G.; Sagnes, I.; Wilde, Y.; De Colombelli, R. Sub-Wavelength Energy

Concentration with Electrically Generated Mid-Infrared Surface Plasmons. *Opt. Express* **2012**, *20*, 13738−13747.
(24) Rusina, A.; Durach, M.; Nelson, K.; Stockman, M. Nanoconcentration of Terahertz Radiation in Plasmonic Waveguides. *Opt. Express* **2008**, *16*, 18576−18589.
(25) Krenz, P. M.; Olmon, R. L.; Lail, B. A.; Raschke, M. B.; Boreman, G. D. Near-Field Measurement of Infrared Coplanar Strip Transmission Line Attenuation and Propagation Constants. *Opt. Express* **2010**, *18*, 21678−21686.
(26) Schnell, M.; Alonso-González, P.; Arzubiaga, L.; Casanova, F.; Hueso, L. E.; Chuvilin, A.; Hillenbrand, R. Nanofocusing of Mid-Infrared Energy with Tapered Transmission Lines. *Nat. Photonics* **2011**, *5*, 283−287.
(27) Sarriugarte, P.; Schnell, M.; Alonso-González, P.; Arzubiaga, L.; Golmar, F.; Casanova, F.; Hueso, L. E.; Hillenbrand, R. Propagation and Nanofocusing of Infrared Surface Plasmons on Tapered Transmission Lines: Influence of the Substrate. *Opt. Commun.* **2012**, *285*, 3378−3382.
(28) Kim, Z. H.; Leone, S. R. Polarization-Selective Mapping of near-Field Intensity and Phase around Gold Nanoparticles Using Apertureless Near-Field Microscopy. *Opt. Express* **2008**, *16*, 1733−1741.
(29) Esteban, R.; Vogelgesang, R.; Dorfmüller, J.; Dmitriev, A.; Rockstuhl, C.; Etrich, C.; Kern, K. Direct Near-Field Optical Imaging of Higher Order Plasmonic Resonances. *Nano Lett.* **2008**, *8*, 3155−3159.
(30) Einsle, J. F.; Bouillard, J.-S.; Dickson, W.; Zayats, A. V. Hybrid FIB Milling Strategy for the Fabrication of Plasmonic Nanostructures on Semiconductor Substrates. *Nanoscale Res. Lett.* **2011**, *6*, 572.
(31) Dayen, J.-F.; Faramarzi, V.; Pauly, M.; Kemp, N. T.; Barbero, M.; Pichon, B. P.; Majjad, H.; Begin-Colin, S.; Doudin, B. Nanotrench for Nano and Microparticle Electrical Interconnects. *Nanotechnology* **2010**, *21*, 335303.
(32) Huang, J.-S.; Callegari, V.; Geisler, P.; Brüning, C.; Kern, J.; Prangsma, J. C.; Wu, X.; Feichtner, T.; Ziegler, J.; Weinmann, P.; Kamp, M.; Forchel, A.; Biagioni, P.; Sennhauser, U.; Hecht, B. Atomically Flat Single-Crystalline Gold Nanostructures for Plasmonic Nanocircuitry. *Nat. Commun.* **2010**, *1*, 150.
(33) Marshall, M. M.; Yang, J.; Hall, A. R. Direct and Transmission Milling of Suspended Silicon Nitride Membranes with a Focused Helium Ion Beam. *Scanning* **2012**, *34*, 101−106.
(34) Bell, D. C.; Lemme, M. C.; Stern, L. A.; Williams, J. R.; Marcus, C. M. Precision Cutting and Patterning of Graphene with Helium Ions. *Nanotechnology* **2009**, *20*, 455301.
(35) Lemme, M. C.; Bell, D. C.; Williams, J. R.; Stern, L. A.; Baugher, B. W. H.; Jarillo-Herrero, P.; Marcus, C. M. Etching of Graphene Devices with a Helium Ion Beam. *ACS Nano* **2009**, *3*, 2674−2676.
(36) Wang, Y.; Boden, S. A.; Bagnall, D. M.; Rutt, H. N.; de Groot, C. H. Helium Ion Beam Milling to Create a Nano-Structured Domain Wall Magnetoresistance Spin Valve. *Nanotechnology* **2012**, *23*, 395302.
(37) Melli, M.; Polyakov, A.; Gargas, D.; Huynh, C.; Scipioni, L.; Bao, W.; Ogletree, D. F.; Schuck, P. J.; Cabrini, S.; Weber-Bargioni, A. Reaching the Theoretical Resonance Quality Factor Limit in Coaxial Plasmonic Nanoresonators Fabricated by Helium Ion Lithography. *Nano Lett.* **2013**, *13*, 2687−2691.
(38) Wang, Y.; Abb, M.; Boden, S. A.; Aizpurua, J.; de Groot, C. H.; Muskens, O. L. Ultrafast Nonlinear Control of Progressively Loaded, Single Plasmonic Nanoantennas Fabricated Using Helium Ion Milling. *Nano Lett.* **2013**, *13*, 5647−5653.
(39) Schnell, M.; Garcia-Etxarri, A.; Huber, A. J.; Crozier, K.; Aizpurua, J.; Hillenbrand, R. Controlling the Near-Field Oscillations of Loaded Plasmonic Nanoantennas. *Nat. Photonics* **2009**, *3*, 287−291.
(40) Schnell, M.; Garcia-Etxarri, A.; Huber, A. J.; Crozier, K. B.; Borisov, A.; Aizpurua, J.; Hillenbrand, R. Amplitude- and Phase-Resolved Near-Field Mapping of Infrared Antenna Modes by Transmission-Mode Scattering-Type Near-Field Microscopy. *J. Phys. Chem. C* **2010**, *114*, 7341−7345.
(41) Schnell, M.; Garcia-Etxarri, A.; Alkorta, J.; Aizpurua, J.; Hillenbrand, R. Phase-Resolved Mapping of the Near-Field Vector and Polarization State in Nanoscale Antenna Gaps. *Nano Lett.* **2010**, *10*, 3524−3528.
(42) Ocelic, N.; Huber, A.; Hillenbrand, R. Pseudoheterodyne Detection for Background-Free Near-Field Spectroscopy. *Appl. Phys. Lett.* **2006**, *89*, 101124.
(43) Hillenbrand, R.; Keilmann, F.; Hanarp, P.; Sutherland, D. S.; Aizpurua, J. Coherent Imaging of Nanoscale Plasmon Patterns with a Carbon Nanotube Optical Probe. *Appl. Phys. Lett.* **2003**, *83*, 368−370.
(44) Alonso-González, P.; Albella, P.; Golmar, F.; Arzubiaga, L.; Casanova, F.; Hueso, L. E.; Aizpurua, J.; Hillenbrand, R. Visualizing the Near-Field Coupling and Interference of Bonding and Anti-Bonding Modes in Infrared Dimer Nanoantennas. *Opt. Express* **2013**, *21*, 1270−1280.
(45) Novotny, L.; Hecht, B. *Principles of Nano-Optics*; Cambridge University Press: Cambridge, 2006.
(46) Maier, S. A. Effective Mode Volume of Nanoscale Plasmon Cavities. *Opt. Quantum Electron.* **2006**, *38*, 257−267.